The effect of temperature and humidity fluctuations on the liquid water path of non-precipitating closed cell stratocumulus clouds

Stephan R. de Roode[1] and Alexander Los

Royal Netherlands Meteorological Institute (KNMI)

Revised manuscript submitted to the Q. J. R. Meteor. Soc., 18 December 2007

[1]Corresponding author address: Stephan R. de Roode, roode@knmi.nl, Royal Netherlands Meteorological Institute (KNMI), PO Box 201, 3730 AE De Bilt, The Netherlands.

Abstract

The spatial variability of the liquid water path (LWP) is analyzed from a large-eddy simulation of the diurnal cycle of stratocumulus clouds as observed during FIRE I. In stratocumulus clouds the temperature and the total specific humidity cannot fluctuate independently but are tightly connected to fluctuations in the liquid water potential temperature. If the latter are relatively small, a strong positive correlation between the temperature and the total specific humidity can be expected. The effect of temperature fluctuations on the magnitude of liquid water fluctuations must be considered to properly compute the LWP distribution in stratocumulus clouds.

The simulated stratocumulus cloud fields are used to compute the albedo inhomogeneity factor χ according to the effective thickness approach. During the day the mean LWP decreases due to shortwave radiative warming. Also, the probability density function for the LWP becomes positively skewed due to cumuli that have their base well below the mean stratocumulus cloud base height. For this situation the inhomogeneity factor χ obtains a minimum value of about 0.85. For a solid (unbroken) cloud with an assumed Gaussian distribution for the optical depth we find that the minimum albedo bias factor will be about 0.8. This minimum value for the inhomogeneity factor, and the LES results are larger than reported from FIRE I observations by Cahalan et al. (1994).

1. Introduction

A cloud layer which exhibits horizontal variations in the liquid water path (LWP) will typically have a lower cloud albedo than a plane parallel cloud that has exactly the same volume mean cloud liquid water path and microphysical structure (Harshvardhan and Randall, 1985). This plane parallel albedo bias arises because the albedo of a cloudy column is a convex function of the cloud optical depth.

Large-scale models that do not have information on the subgrid variability of the liquid water path should therefore correct for the albedo bias factor as plane parallel clouds will invariably have larger cloud albedos. Cahalan et al. (1994) analysed time series of marine stratocumulus LWPs observed off the coast of California during the FIRE I experiment. They showed that the observed albedos can be reproduced with the plane-parallel calculation if an effective cloud optical depth τ_{eff} is used, according to $\tau_{eff} = \chi\tau$. During FIRE, the inhomogeneity factor was estimated $\chi = 0.7$ (Cahalan et al., 1994). The use of this reduction factor, which is also refered to as the effective thickness approximation (ETA), was implemented in the ECMWF model by Tiedtke (1996). However, Pincus et al. (1999) studied ship observations and satellite imagery of stratocumulus in the same region and found a much smaller albedo bias effect. The use of a constant reduction factor is questionable as its precise value depends on the mean and the variance of the cloud optical depth, which are controled by the boundary layer turbulence and the large-scale atmospheric circulation (Barker et al., 1996; Los and Duynkerke, 2001; Rossow et al., 2002; Bäuml et al., 2004).

The McICA (Monte Carlo Independent Column Approximation) method is a fundamentally different approach to incorporate the effect of cloud horizontal inhomogeneity on radiation

(Barker et al., 2002; Barker and Räisänen, 2004; Pincus et al., 2003; Räisänen et al., 2004). This method is based on the generation of a cloud field on a column-by-column basis while conserving the same value for the mean column liquid water path. The cloud generator uses information about layer cloud fraction, vertical overlap of cloud fraction and cloud condensate for adjacent layers, and density functions describing horizontal variations in cloud water content. The Independent Column Approximation (ICA) assumes that the radiative transfer can be computed for every single subcolumn, which eliminates the need to correct for the albedo bias effect. The accuracy of the McICA procedure critically depends on a precise estimation of the subgrid variability of the liquid water path and the cloud fraction.

In this study we analyse the effect of humidity and temperature fluctuations on the cloud liquid water variability. We analyse results from a large-eddy simulation (LES) of the the diurnal cycle of FIRE I stratocumulus. This case was set up as a model intercomparison case in the framework of the EUROCS project (Duynkerke et al., 2004). To allow the formation of mesoscale fluctuations by boundary-layer turbulence the simulation was performed on a large horizontal domain of 25.6×25.6 km^2 (De Roode et al., 2004). The motivation of this research can perhaps be best illustrated from the LES results displayed in Figure 1. It is clear that that the modeled LWP, the in-cloud total water specific humidity, the temperature and the liquid water content exhibit nearly identical spatial structures. Section 2 discusses in more detail some statistics of the LES results and compares them to observations reported by Wood and Taylor (2001). The effect of temperature fluctuations on liquid water fluctuations is discussed in sections 3 and 4. The diurnal variation of the inhomogeneity factor χ is computed from simulated FIRE I stratocumulus fields and is presented in section 5. Section 6 summarizes and discusses

the major findings.

2. Large-eddy simulation of the diurnal cycle of stratocumulus as observed during FIRE I

a. Experimental setup

The diurnal cycle of the FIRE I stratocumulus case is investigated from results obtained with the dutch atmospheric LES (DALES) model. A large horizontal domain (25.6 $\times$ 25.6 $\times$ 1.2 km^3) was used with a horizontal (vertical) grid space of 100 (20) m. The model solves prognostic equations for the liquid water potential temperature $\theta_l = \theta - \frac{L_v}{c_p \Pi} q_l$, the total water content $q_t = q_v + q_l$ and the u, v and w components of the wind velocities. Here $\Pi = T/\theta$ indicates the Exner function, q_v (q_l) is the (liquid water) specific humidity, θ is the potential temperature, L_v is the latent heat of vaporization, c_p is the isobaric specific heat for dry air, and $\epsilon_I = 1/\epsilon - 1 \approx 0.608$, where $\epsilon = R_d/R_v$ the ratio of the specific gas constants for dry air and water vapor. Note that in the absence of cloud liquid water, $\theta_l = \theta$. The LES model does not take into account drizzle, in which case the quantities θ_l and q_t are conserved for adiabatic processes that involve condensation or evaporation. The simulated stratocumulus cloud layer studied here can therefore be best regarded as a polluted cloud, which is less likely to produce precipitation than stratocumulus in a very clear environment. The grid-box mean of the liquid water content is diagnosed from the grid-box mean values of θ_l and q_t. We use overbars to indicate the slab average over the horizontal domain of the model, and primes to denote the deviation from the horizontal slab mean, e.g. $\overline{\theta_l}$ and θ_l'.

The initial (thermo-) dynamic state was based on radiosonde observations of temperature and relative humidity vertical profiles collected during the FIRE I stratocumulus experiment (Duynkerke et al., 2004). The effects of large-scale horizontal advection and radiative flux divergence in the free atmosphere were accounted for by prescribed fixed, height-dependent tendencies. In addition, the large-scale subsidence rate was prescribed.

b. Simulated evolution of the cloud layer

The simulated evolution of the stratocumulus cloud boundaries are displayed in Figure 2. The cloud top is capped by a very strong inversion. The gradual increase of the cloud top height during the night and a lowering during the day reflects a competition between the large-scale subsidence and the entrainment rate. The boundary layer height is in a steady state if the entrainment rate balances the large-scale subsidence. The latter tends to advect the boundary layer height downwards, whereas turbulent mixing of free atmosphere air into the boundary layer acts to counteract this process. During the day absorption of solar radiation warms the cloud layer which causes a weak stable stratification near the base of the cloud. As a result the turbulence intensity in the cloud layer weakens and the entrainment rate decreases.

Because the cloud top is capped by a stable inversion layer, the standard error of the cloud top height is quite small indicating a rather homogeneous spatial distribution of cloud top heights. On the contrary, the mean cloud base height shows much larger fluctuations with time. However, notice that after about 10 hours simulation time thermals that are triggered from the surface reach saturation at almost a constant height, as can be seen from a nearly constant lowest cloud-base height.

The mean cloud liquid water path (LWP) is defined by

$$\overline{LWP} = \rho_0 \int_0^{z_{top}} \overline{q_l}(z) dz, \tag{1}$$

with ρ_0 the mean air density (which is necessary if q_l has units kg/kg rather than kg m^{-3}), and z_{top} the top of the LES domain. The mean LWP is maximum during the night and minimum during the day. Notice the relatively large maximum LWPs in the LES domain during the simulation time, which can be explained from cloud columns that have a relatively low cloud base and a top close to the mean inversion layer height. Thumbnail plots of the simulated liquid water path probability density functions (PDFs) are displayed in Figure 3.

Figure 4 shows the temporal evolution of the skewness for the liquid water path,

$$S_{LWP} = \frac{\overline{LWP'^3}}{\overline{LWP'^2}^{3/2}} \tag{2}$$

and likewise for the total specific humidity (S_{q_t}) in the middle of the cloud layer at 450 m. During the first night (0-8 Local Time) S_{LWP} is negative, but during the second night its near zero values indicate that the PDF of the LWP is more or less symmetric. The positive values for S_{LWP} during daytime are due to thermals that become saturated well below the mean cloud base height. Positive values S_{LWP} are accompanied by positive values for S_{q_t} in the middle of the cloud layer. These results are similar to FIRE I observations analyzed by Wood and Taylor (2001). They showed that for the case where the mean LWP is small and the cloud-base height distribution is fairly broad the observations exhibit a positively skewed distribution for the LWP.

c. Spectral properties

Figure 5 shows energy density spectra of the LWP at four different times. These spectra were obtained from a Fourier transformation, which provides a two-dimensional matrix of the (co-)spectral energy, $E(k_x, k_y)$. The spectral energy density $S = E/dk$, with dk the wavenumber interval. The energy density spectra shown in the figure are plotted as a function of the wavenumber $k = \sqrt{k_x^2 + k_y^2}$. The minimum wavenumber $k_{min} = 1/25600$ m^{-1} is determined by the horizontal domain size of the LES model. From the start of the simulation the LWP variance at the largest length scales gradually grows with time. After 36 hours simulation time the LWP spectral energy is maximum at the smallest wavenumber. Wood and Hartmann (2006) found from MODIS data of marine low cloud over the eastern subtropical oceans that the LWP spatial variance is dominated by horizontal scales of 10-50 km, where larger length scales are indicative for mesoscale cellular convection. Note that in a large-eddy simulation the growth of fluctuations at the mesoscales is due to turbulence convection only (Jonker et al., 1999; De Roode et al., 2004).

Energy density spectra for T, q_t and θ_v in the middle of the subcloud layer and the middle of cloud layer at t=36 Local Time are shown in Figure 6. Figure 6c shows that the temperature and total specific humidity exhibit a strong positive correlation in the cloud layer. Observations collected in the subcloud layer of various stratocumulus cases analyzed by Wood and Taylor (2001) show negative correlations at scales larger than the boundary layer depth. The LES fields in the subcloud layer also indicate negative correlations between the total specific humidity and temperature at all length scales (see Figure 6c). This result can be qualitatively understood from the vertical flux profiles (not shown here). In the simulations, the buoyancy flux tends to become

negative above the middle of the subcloud layer up to the cloud base height, whereas the total specific humidity flux is positive from the surface to the cloud top. These flux profiles are quite common in stratocumulus cloud layers (Nicholls, 1984). In clear, unsaturated air fluctuations of the virtual potential temperature are, to a good approximation, given by

$$\theta_v' = T' + 0.61\overline{\theta_v}q'. \tag{3}$$

Therefore, for parcels with $\theta_v' < 0$ and $q' > 0$, this means that $T' < 0$ in order to satisfy (3). Note that in the subcloud layer the spectral variance of the temperature is slightly larger than that of the virtual potential temperature. From the expression above we can derive

$$\theta_v'^2 = T'^2 + (0.61\overline{\theta_v})^2 q'^2 + 2 \cdot 0.61\overline{\theta_v}T'q', \tag{4}$$

from which directly follows that the temperature and the specific humidity must be negatively correlated if the sum of their respective (spectral) variances is larger than the variance of θ_v.

3. Temperature and humidity correlations in the stratocumulus cloud layer

a. LES results

Figure 7 shows that the LWP and q_t in the middle of the cloud layer (at 450 m) are well correlated. Relatively large q_t values correspond to larger LWPs, and vice versa. During the day the slightly curved shape in the scatter plot of q_t and LWP fluctuations is due to a more inhomogeneous cloud structure with cumulus clouds penetrating a relatively thin stratocumulus layer above.

Figure 8 shows scatter plots of T' and q_t' in the middle of the cloud layer. Relatively moist air parcels appear to be relatively warm, and vice versa. In particular during night-time T' and q_t' satisfy an approximate linear relationship,

$$T' = c_{qT} q_t', \tag{5}$$

where the factor c_{qT} represents the slope of the linear fit shown in the figure.

To calculate q_l' fluctuations from q_t' fluctuations one needs to account for fluctuations of the saturation specific humidity q_{sat}' according to

$$q_l' = q_t' - q_v' = q_t' - q_{sat}'(T). \tag{6}$$

Fluctuations in the saturation specific humidity q_{sat} can be calculated from temperature fluctuations according to the Clausius-Clapeyron relation (Nicholls, 1984)

$$q_{sat}' = \left(\frac{dq_{sat}}{dT} \right) T' = \gamma T', \tag{7}$$

with $\gamma \equiv \frac{dq_{sat}}{dT}$. In the middle of the cloud layer the mean temperature is about 12° C and $\gamma \approx 0.6$ g kg^{-1} K^{-1}. Using (7), and substitution of (5) in (6) yields an expression for q_l' which depends on q_t' only,

$$q_l' = q_t' \left(1 - \gamma c_{qT}\right) \equiv \beta q_t', \tag{8}$$

which defines the β factor. Figure 9 shows that the PDF for q_t is much broader than for q_l, which indicates that $\beta < 1$.

The fact that q_t and T are well correlated can be understood by considering the expression for the liquid water potential temperature fluctuations,

$$\theta_l' = \theta' - \frac{L_v}{c_p} q_l' = T'(1 + \frac{L_v}{c_p}\gamma) - \frac{L_v}{c_p} q_t', \tag{9}$$

where we used Eqs. (6), (7) and the approximation $T' \approx \theta'$. Temperature fluctuations can therefore be written as

$$T' = A_w \theta_l' + B_w q_t', \tag{10}$$

which explains why in the cloud layer T and q_t can not vary independently. The factor $A_w = (1 + \frac{L_v}{c_p}\gamma)^{-1}$ depends weakly on the temperature and has a value of about 0.4 in the middle of the cloud layer, and $B_w = \frac{L_v}{c_p}(1 + \frac{L_v}{c_p}\gamma)^{-1} \approx 1000$ K.

Figure 10 shows that the variance $A_w^2 \overline{\theta_l'^2}$ is much smaller than $\overline{T'^2}$. In that case, one may approximate

$$T' \approx B_w q_t'. \tag{11}$$

The slope in the scatter plot of q_t' and T' for the nighttime case displayed in Figure 8 is about equal to B_w.

In case θ_l fluctuations can be neglected, a comparison of (5) to (11) shows that the β factor can be expressed as,

$$\beta|_{\theta_l'=0} = (1 - \gamma B_w). \tag{12}$$

In the middle of the cloud layer $\beta|_{\theta_l'=0} \approx 0.4$. Thus, according to (12) the magnitude of q_l fluctuations is more than halved if θ_l fluctations are ignored rather than T fluctuations. We have used the LES cloud fields to directly compute the β factor as defined by Eq. (8). The factor c_{qT} was obtained from a linear fit of the total specific humidity and temperature in the middle of the cloud layer. Figure 11 shows a weak diurnal variation of the β factor. Overall, the β factor has values rather close to 0.4. This means that for the FIRE I case the effect of temperature fluctuations on liquid water fluctuations should not be neglected.

b. Analysis of flux profiles

Vertical turbulent fluxes of θ_l and q_t at the stratocumulus cloud top can be diagnosed straightforwardly from the so-called flux-jump relation (Lilly, 1968),

$$\overline{w'\psi'}_T = -w_e \times \Delta\psi, \tag{13}$$

with $\Delta\psi$ the jump of $\psi \in \{q_t, \theta_l\}$ across the inversion and w_e the entrainment rate. The entrainment rate (ms^{-1}) is the rate with which turbulent eddies mix air from just above the inversion air into the boundary layer.

If the air above the stratocumulus layer is clear, then the top of the stratocumulus cloud is cooled because more longwave radiation is emitted than is absorbed from above. The vertical divergence of the net longwave radiative flux near the top of the cloud layer is typically about $\Delta F_L \approx 70$ W/m^2, and occurs in a layer of only a few tenths of meters thick. Just below the layer which is radiatively cooled (we will indicate fluxes at this level by a primed subscript $_{T'}$) the vertical turbulent flux of θ_l can then be expressed as (Nicholls, 1984; Stevens, 2002),

$$\overline{w'\theta'_l}_{T'} = -w_e \Delta\theta_l + \frac{\Delta F_L}{\rho_0 c_p}. \tag{14}$$

This formula is valid for a boundary layer that is in a quasi-steady state, meaning that the temporal change of the mean of θ_l and q_t is constant with height. Furthermore we assume that the depth of the radiatively cooled layer is sufficiently small in order to approximate the total humidity flux $\overline{w'q'_t}_{T'}$ by the flux-jump formula (13).

Using Eq. (10) we can express the temperature flux in the cloud layer as

$$\overline{w'T'} = A_w \overline{w'\theta'_l} + B_w \overline{w'q'_t}. \tag{15}$$

To explore which of the two fluxes on the rhs of (15) dominates the temperature flux we define the ratio R,

$$R \equiv \frac{\overline{w'T'}}{B_w \overline{w'q_t'}} = \frac{A_w \overline{w'\theta_l'}}{B_w \overline{w'q_t'}} + 1. \tag{16}$$

The quantity R is unity if the contribution of the liquid water potential temperature flux to the temperature flux is zero. If we use an entrainment parameterization, the value of R near the cloud top can be computed. Moeng (2000) presents an entrainment parameterization for stratocumulus clouds,

$$w_e = \frac{0.2\overline{w'\theta'}_0 + \frac{\Delta F_L}{\rho_0 c_p}[2.5 - 2\exp(-\sqrt{b_m LWP})]}{\Delta\theta_l}, \tag{17}$$

with $b_m = 0.9 m^2 kg^{-1}$. Note that Moeng's parameterization depends only on $\Delta\theta_l$, the potential temperature flux at the surface $\overline{w'\theta'}_0$, and ΔF_L, whereas other entrainment parameterizations reviewed by Stevens (2002) do also depend on Δq_t and the humidity flux at the surface $\overline{w'q'_{t0}}$. Substitution of Eq. (17) in (14) yields,

$$\overline{w'\theta'_l}_{T'} = -0.2\overline{w'\theta'}_0 - \frac{\Delta F_L}{\rho_0 c_p}[1.5 - 2\exp(-\sqrt{b_m LWP})]. \tag{18}$$

Using the entrainment rate parameterization (17) and the flux-jump relation (13) R can be computed as a function of the inversion jumps $\Delta\theta_l$ and Δq_t. We used $\overline{w'\theta'}_0 = 0.01$ Kms^{-1}, $\Delta F_L = 70$ Wm^{-2}, and $LWP = 0.150$ kg m^{-2} to calculate the results presented in Figure 12. The inversion jumps of the FIRE I stratocumulus case are also depicted in the figure. In particular for humidity jumps $\Delta q_t < -2$ g kg^{-1}, R is positive and is rather close to unity. This implies that near the top of the cloud layer the temperature flux will be dominated by the total humidity flux. In that case the correlation between the temperature and the total specific humidity will likely be positive.

4. A simple model to predict LWP fluctations from the total specific humidity

On the basis of the LES results we develop a simple model to predict the PDF of LWP that uses an assumed distribution of total specific humidity fluctuations. In a large-scale model the latter may be computed by parameterizing the prognostic equation for the total specific humidity variance (Tompkins, 2002).

First of all, we assume that the vertical profile of the liquid water content in any cloudy subcolumn in the LES domain is given by a "pseudo-adiabatic" mean liquid water vertical gradient α that is based on the actual modeled mean liquid water path $\overline{LWP}$. With aid of (1) the slope α can be expressed as,

$$\alpha = \frac{2\overline{LWP}}{\rho_0 \overline{H}^2} \qquad \Longleftrightarrow \qquad \overline{LWP} = \frac{1}{2}\rho_0 \alpha \overline{H}^2, \tag{19}$$

with $\overline{H} = \overline{z_t} - \overline{z_b}$ the mean cloud-layer depth. For a vertically well-mixed stratocumulus layer α will be close to the moist-adiabat. For a constant slope α the pseudo-adiabatic maximum mean liquid water is proportional to the mean cloud depth height,

$$\overline{q_l}_{max} = \alpha \overline{H}. \tag{20}$$

As a next step, we have to predict the vertical variation of liquid water fluctuations in cloudy subcolumns. From the LES results we have computed the subcolumn vertical mean liquid water fluctuation according to,

$$[q_l'](x,y) = \frac{\int_{z_{base}(x,y)}^{z_{top}(x,y)} [q_l(x,y,z) - \overline{q_l}(z)]dz}{z_{top}(x,y) - z_{base}(x,y)}. \tag{21}$$

Fig. 13 shows that $[q_l']$ correlates well with the subcolumn liquid water content fluctuation q_l' in the middle of the mean cloud layer. We use this result to assume that the liquid water content fluctuation in a cloudy subcolumn can be approximated to be constant with height, except near the cloud base where the liquid water content increases linearly with height (see Figure 14 for a schematic).

Third, like Considine et al. (1997), Los and Duynkerke (2000) and Wood and Taylor (2001) we will assume that the stratocumulus cloud-top height variability is negligibly small. According to the LES results shown in Figure 2 this is a justifiable assumption for the FIRE I stratocumulus case. For an arbitrary cloudy subcolumn the maximum liquid water content $q_{l,max}$ can then be written as

$$q_{l,max} = \overline{q_l}_{max} + q_l'. \tag{22}$$

Let us write the local cloud depth as $H = \overline{H} + H'$. Because the vertical gradient α applies to all cloudy subcolumns, $q_{l,max} = \alpha H$, and from (20) it follows

$$H' = \frac{q_l'}{\alpha}. \tag{23}$$

Similar to Eq. (19) the local LWP can be expressed as

$$LWP = \frac{1}{2}\rho_0\alpha(\overline{H} + H')^2 = \frac{\rho_0}{2\alpha}(\alpha\overline{H} + q_l')^2. \tag{24}$$

After subtracting the mean LWP we obtain,

$$LWP' = \rho_0\overline{H}q_l' + \frac{\rho_0 {q_l'}^2}{2\alpha}. \tag{25}$$

With aid of Eq. (8) we can substitute out q_l' fluctuations,

$$LWP' = \rho_0\overline{H}\beta q_t' + \frac{\rho_0\beta^2 {q_t'}^2}{2\alpha}. \tag{26}$$

The first term on the rhs of Eq. (26) gives $LWP' = \rho_0 \overline{H} \beta q_t'$, which is proportional to the area of the parallelogram with height $\overline{H}$ and width $\beta q_t'$. Likewise, with aid of Eqs. (8) and (23) the second term can be rewritten as $LWP' = \rho_0 H' \beta q_t'/2$, which is proportional to the area of the triangle having a height H' and width $\beta q_t'$. If $\beta > 1$, then cloudy subcolumns are relatively moist and cold (or dry and warm), causing liquid water content fluctuations to be enhanced by a local colder (warmer) temperature, and vice versa for $\beta < 1$.

Examples of actual and constructed PDFs for the LWP fluctuations are shown in Figure 3. The total specific humidity fluctations q_t' are taken from the LES results at a height of 450 m, which is at about the middle of the cloud layer. The β factors were computed from linear fits of the temperature and total specific humidity, according to the results shown in Figure 11. The reconstructed PDFs for the LWP agree satisfactorily well with the actual LWP distribution. If we neglect temperature fluctuations by using $\beta = 1$, then the reconstructed PDFs for the LWP become much too broad.

5. Albedo bias

The delta-Eddington radiative transfer equation (Joseph et al., 1976) and the I3RC Monte Carlo model (Cahalan et al., 2005) were used to compute the albedos from instantaneous, hourly simulated FIRE I stratocumulus cloud fields. The delta-Eddington method is a computationally cheap means to compute radiative transfer through a horizontally homogeneous cloud, whereas the Monte Carlo model utilizes the full three-dimensional structure of the cloud field. The delta-Eddington model was used to compute the plane parallel cloud albedo A_{PPH} from the horizontally slab-averaged value of the liquid water path. The optical depth τ of the cloud was

calculated according to

$$\tau = \frac{3}{2}\frac{LWP}{\rho_w r_e}, \tag{27}$$

with ρ_w the density of liquid water and $r_e = 10\mu$ a constant cloud droplet effective radius. To focus on the effect of the cloud structure on the albedo we used a fixed solar zenith angle $\theta_0 = 53^\circ$. More details on the boundary conditions and the model parameters can be found in Duynkerke et al. (2004).

The effect of the horizontal inhomogeneities in the cloud LWP on the mean cloud albedo were assessed from the delta-Eddington model by computing the albedo for all 256$\times$ 256 cloud columns in the LES domain. According to the independent column approximation (ICA) the mean albedo of the horizontally inhomogeneous cloud (A_{ICA}) can then be obtained by horizontally averaging the albedos of all cloud subcolumns. The cloud inhomogeneity factor χ is determined by finding the optical depth τ_{eff} for which its plane parallel albedo corresponds exactly to the mean albedo for a horizontally inhomogeneous cloud according to the ICA approach, $A(\tau_{eff}) = A_{ICA}$ such that

$$\chi = \frac{\tau_{eff}}{\overline{\tau}}. \tag{28}$$

Note that Rossow et al. (2002) define the inhomogeneity factor $\epsilon = 1 - \chi$. The mean cloud albedo (A_{MC}) was also computed using the full three-dimensional liquid water content fields as input for a Monte Carlo radiative transfer model. Note that this model uses the same model parameters as used for the delta-Eddington calculations.

Figure 15 shows that the differences in the inhomogeneity factor χ computed from the delta-Eddington and the Monte Carlo models are less than 0.02. This implies that under the present conditions the detailed three-dimensional spatial distribution of cloud liquid water appears to

be of relatively little importance. Because a fixed solar zenith angle was used to compute the inhomogeneity factor, the temporal variations in χ can be explained only by variations in the mean and the variance of the optical depth. According to the Monte Carlo modeling results, the factor χ has a minimum value of about 0.85 during day-time when the ratio $\sigma_\tau/\overline{\tau}$ is maximum.

To explain these findings Figure 16 displays isolines of the inhomogeneity factor χ as a function of the mean optical depth $\overline{\tau}$ and its standard deviation normalized by the mean value, $\sigma_\tau/\overline{\tau}$. The inhomogeneity factor was computed with the delta-Eddington model where we systematically changed the width of an assumed Gaussian optical depth distribution. Note that for too large values of σ_τ negative values for the optical depth will arise, which can be interpreted as clear air patches in the cloud layer. At this point the factor χ tends to decrease rapidly. The figure shows results only for cloud fractions larger than 0.99. For a given mean value of the optical depth, the inhomogeneity effect becomes increasingly important for larger optical depth variances. We conclude that solid clouds with $\overline{\tau} < 30$ and a Gaussian optical depth distribution will typically have an inhomogeneity factor $\chi > 0.8$.

According to Oreopoulos and Davies (1998) the albedo bias is dependent on the domain size of the cloud field. This is due to the fact that the variance of the liquid water path increases with increasing domain size (De Roode et al., 2004). To investigate this effect from the LES cloud fields, we used the most inhomogeneous cloud field at $t = 36$ Local Time, and divided the LES horizontal domain into smaller subdomains, ranging from 2^2, 2^3, ..., 2^7 grid points. For these subdomains we computed the variance of the optical depth and the inhomogeneity factor χ. To determine the latter, mean plane-parallel albedos were computed for every subdomain cloud field. Next, we averaged every set of equal subdomain size results. It is clear from Figure

17 that the total horizontal mean optical depth variance increases if the subdomain size becomes larger. Also, for subdomain sizes < 10 km the albedo bias effect is insignificant as $\chi > 0.95$.

The inhomogeneity factors computed from the LES cloud fields are significantly larger than the value of about 0.7 found from microwave retrievals of LWP during FIRE I by Cahalan et al. (1994). This does not appear to be caused by an unrealistic simulated cloud structure, as the simulated LWP PDFs compare qualitively well to the FIRE I LWP analyses reported by Wood and Taylor (2001). In addition, the albedo bias values computed from the LES FIRE I cloud fields are in agreement with LES results of other stratocumulus cloud cases discussed by Bäuml et al. (2004). Oreopoulos and Cahalan (2005) studied satellite images of marine stratocumulus regimes, and observed values of χ greater than about 0.85 in July, consistent with the satellite values of Pincus et al. (1999) and Rossow et al. (2002). As illustrated from Figure 16, χ values that do not deviate much from unity are typically associated to overcast grid points. This stresses the significant effect of the cloud fraction on the albedo bias (Barker et al., 1996; Pincus et al., 1999; Rossow et al., 2002; Oreopoulos and Cahalan, 2005).

6. Conclusions

Cloud fields obtained from a large-eddy simulation of the diurnal cycle of FIRE I stratocumulus are studied. It is found that the temperature and the total specific humidity fields in the cloud layer exhibit similar spatial structures as the liquid water path. The positive correlation between the total specific humidity and the temperature in the cloud layer indicates that relatively moist air is typically warmer and vice versa. Liquid water content fluctuations are found to be much smaller than the total specific humidity fluctuations, which is attributed to the temperature effect

on the saturation specific humidity.

We present a model that takes into account the temperature effect on the saturation specific humidity. In this model we calculate liquid water fluctuations from the total specific humidity and a scale factor β. The β factor gives a measure of the temperature effect on liquid water fluctuations. In the limit of vanishing temperature fluctuations $\beta = 1$. However, if liquid water potential temperature fluctuations are negligibly small it can be shown that β should be much smaller. In particular, $\beta \approx 0.4$ for the FIRE I stratocumulus case. The reduced β factor value may perhaps also be a better assumption for other stratocumulus cases. In particular, this will be the case if positive liquid water potential temperature fluctuations caused by entrainment mixing of higher θ_l values from just above the inversion are strongly diminished by longwave radiative cooling near the cloud top.

The LES results are used to develop a parameterization for liquid water path subcolumn fluctuations from total specific humidity fluctuations only. In a large-scale model the latter can be computed from solving the prognostic equation for the total specific humidity variance (Tompkins, 2002). The presented model uses the β factor and is capable to reproduce the actual LWP PDFs rather satisfactorily. Neglecting the effect of temperature fluctuations leads to LWP PDFs that are too broad.

The LES fields are also used to compute the difference between the albedo computed from the horizontal mean cloud liquid water path, and the albedo based on the actual horizontally inhomogeneous cloud field according to the Independent Column Approximation. This so-called albedo bias effect appears to be insignificant if the simulated clouds are optically thick, but becomes increasingly important for clouds that have a large ratio of the optical depth standard

deviation to its mean value, $\sigma_\tau/\overline{\tau}$. This is typically the case for stratocumulus during day-time. The minimum value for the inhomogeneity factor as computed from the LES stratocumulus cloud fields is about $\chi \sim 0.85$.

With a delta-Eddington model we calculated the inhomogeneity factor χ for a solid (unbroken) cloud layer with an assumed Gaussian optical depth distribution. We found a minimum value for χ of about 0.8. If the ratio of the optical depth standard deviation to its mean value decreases, the inhomogeneity factor becomes close to unity. Because the liquid water path variance tends to increase with increasing horizontal grid size, the inhomogeneity factor will therefore generally depend on the horizontal domain size of the large-scale model (Oreopoulos and Davies, 1998). Because of this strong dependence of the albedo bias on the optical depth variance the application of a constant cloud inhomogeneity correction factor in a solar radiative transfer scheme seems rather crude. It calls for a more distinct approach like McICA that directly takes into account the subgrid variability of the liquid water path. From the delta-Eddington calculation for clouds with an assumed Gaussian optical depth distribution we also noticed a sharp decrease in the inhomogeneity factor χ if clear air columns are allowed in the cloud layer. This demonstrates that besides the detailed spatial liquid water distribution of the cloud, the cloud fraction is as important for an accurate computation of the solar radiative transfer.

The cloud albedo bias is principly due to fluctuations in the cloud optical depth. If in a GCM the variance $\overline{q_t'^2}$ is computed, it can be straightforwardly converted to the variance of the LWP. If we neglect the second term on the rhs of Eq. (26), $\overline{LWP'^2}$ may be approximated by

$$\overline{LWP'^2} = (\rho_0 \overline{H} \beta)^2 \overline{q_t'^2}. \tag{29}$$

For a constant cloud droplet effective radius the variance of the optical depth becomes,

$$\overline{\tau'^2} = \left(\frac{3\rho_0 \overline{H}\beta}{2\rho_w r_e}\right)^2 \overline{q_t'^2}, \tag{30}$$

where we used Eq. (27). A more accurate estimation of $\overline{\tau'^2}$ can be made if one takes into account the variation of microphysical properties with height (Los and Duynkerke, 2000; Jeffery and Austin, 2003).

Acknowledgement This research project was carried out in the framework the Dutch National Research Programme Climate changes Spatial Planning (http://www.klimaatvoorruimte.nl). This work was sponsored by the National Computing Facilities Foundation (NCF) for the use of supercomputer facilities.

References

Barker, H. W., R. Pincus, and J. Morcrette, 2002: The Monte Carlo Independent Column Approximation: Application within large-scale models. *Proceedings from the GCSS Workshop*, Kananaskis,Alberta,Canada.

Barker, H. W. and P. P. Räisänen, 2004: Radiative sensitivities for cloud geometric properties that are unresolved by conventional GCMs. *Q. J. R. Meteorol. Soc.*, **130**, 2069–2086.

Barker, H. W., B. A. Wielicki, and L. Parker, 1996: A parameterization for computing grid-averaged solar fluxes for inhomogeneous marine boundary layer clouds. Part II: Validation using satellite data. *J. Atmos. Sci.*, **53**, 2304–2316.

Bäuml, G., A. Chlond, and E. Roeckner, 2004: Estimating the PPH-bias for simulations of convective and stratiform clouds. *Atm. Res.*, **72**, 317–328.

Cahalan, R. F., L. Oreopoulos, A. Marshak, K. F. Evans, A. B. Davis, R. Pincus, K. H. Yetzer, B. Mayer, R. Davies, T. P. Ackerman, H. W. Barker, E. E. Clothiaux, R. G. Ellingson, M. J. Garay, E. Kassianov, S. Kinne, A. Macke, W. O'Hirok, P. T. Partain, S. M. Prigarin, A. N. Rublev, G. L. Stephens, F. Szczap, E. E. Takara, T. Várnai, G. Wen, and T. B. Zhuravleva, 2005: The I3RC: Bringing together the most advanced radiative transfer tools for cloudy atmospheres. *Bull. Amer. Meteorol. Soc.*, **86**, 1275–1293.

Cahalan, R. F., W. Ridgway, W. J. Wiscombe, S. Gollmer, and Harshvardhan, 1994: Independent pixel and Monte-Carlo estimates of stratocumulus albedo. *J. Atmos. Sci.*, **51**, 3776–3790.

Considine, G., J. A. Curry, and B. Wielicki, 1997: Modeling cloud fraction and horizontal variability in marine boundary layer clouds. *J. Geophys. Res.*, **102**, 13517–13525.

De Roode, S. R., P. G. Duynkerke, and H. J. J. Jonker, 2004: Large eddy simulation: How large is large enough? *J. Atmos. Sci.*, **61**, 403–421.

Duynkerke, P. G., S. R. de Roode, M. C. van Zanten, J. Calvo, J. Cuxart, S. Cheinet, A. Chlond, H. Grenier, P. J. Jonker, M. Köhler, G. Lenderink, D. Lewellen, C.-L. Lappen, A. P. Lock, C.-H. Moeng, F. Müller, D. Olmeda, J.-M. Piriou, E. Sanchez, and I. Sednev, 2004: Observations and numerical simulations of the diurnal cycle of the EUROCS stratocumulus case. *Q. J. R. Meteorol. Soc.*, **130**, 3269–3296.

Harshvardhan and D. A. Randall, 1985: Comments on "the parameterization of radiation for numerical weather prediction and climate models". *Mon. Weather Rev.*, **113**, 1832–1833.

Jeffery, C. A. and P. H. Austin, 2003: Unified treatment of thermodynamic and optical variability in a simple model of unresolved low clouds. *J. Atmos. Sci.*, **60**, 1621–1631.

Jonker, H. J. J., P. G. Duynkerke, and J. W. M. Cuijpers, 1999: Mesoscale fluctuations in scalars generated by boundary layer convection. *J. Atmos. Sci.*, **56**, 801–808.

Joseph, J. H., W. J. Wiscombe, and J. A. Weinman, 1976: The delta-Eddington approximation for radiative flux transfer. *J. Atmos. Sci.*, **33**, 2452–2459.

Lilly, D., 1968: Models of cloud-topped mixed layers under a strong inversion. *Q. J. R. Meteorol. Soc.*, **94**, 292–309.

Los, A. and P. G. Duynkerke, 2000: Microphysical and radiative properties of inhomogeneous stratocumulus: Observations and model simulations. *Q. J. R. Meteorol. Soc.*, **126**, 3287–3307.

— 2001: Parametrization of solar radiation in inhomogeneous stratocumulus: Albedo bias. *Q. J. R. Meteorol. Soc.*, **127**, 1593–1614.

Moeng, C.-H., 2000: Entrainment rate, cloud fraction and liquid water path of PBL stratocumulus clouds. *J. Atmos. Sci.*, **57**, 3627–3643.

Nicholls, S., 1984: The dynamics of stratocumulus: Aircraft observations and comparisons with a mixed layer model. *Q. J. R. Meteorol. Soc.*, **110**, 783–820.

Oreopoulos, L. and R. F. Cahalan, 2005: Cloud inhomogeneity from MODIS. *J. Climate*, **18**, 5110–5124.

Oreopoulos, L. and R. Davies, 1998: Plane parallel albedo biases from satellite observations. Part I: Dependence on resolution and other factors. *J. Climate*, **11**, 919–932.

Pincus, R., H. W. Barker, and J. J. Morcrette, 2003: A fast, flexible, approximate technique for computing radiative transfer in inhomogeneous cloud fields. *J. Geophys. Res.*, **108**.

Pincus, R., S. A. McFarlane, and S. A. Klein, 1999: Albedo bias and the horizontal variability of clouds in subtropical marine boundary layers: Observations from ship and satellites. *J. Geophys. Res.*, **104**, 6183–6191.

Räisänen, P., H. W. Barker, J. L. M. F. Khairoutdinov, and D. A. Randall, 2004: Stochastic generation of subgrid-scale cloudy columns for large-scale models. *Q. J. R. Meteorol. Soc.*, **130**, 2047–2067.

Rossow, W. B., C. Delo, and B. Cairns, 2002: Implications of the observed mesoscale variations of clouds for the Earth's radiation budget. *J. Climate*, **15**, 557–585.

Stevens, B., 2002: Entrainment in stratocumulus-topped mixed layers. *Q. J. R. Meteorol. Soc.*, **128**, 2663–2690.

Tiedtke, M., 1996: An extension of cloud-radiation parameterization in the ecmwf model: The representation of subgrid-scale variations of optical depth. *Mon. Weather Rev.*, **124**, 745–750.

Tompkins, A. M., 2002: A prognostic parameterization for the subgrid-scale variability of water vapor and clouds in large-scale models and its use to diagnose cloud cover. *J. Atmos. Sci.*, **59**, 1917–1942.

Wood, R. and D. L. Hartmann, 2006: Spatial variability of liquid water path in marine low cloud: The importance of mesoscale cellular convection. *J. Climate*, **19**, 1748–1764.

Wood, R. and J. P. Taylor, 2001: Liquid water path variability in unbroken marine stratocumulus cloud. *Q. J. R. Meteorol. Soc.*, **127**, 2635–2662.

Figure captions

Figure 1: Grey-scale plots of the instantaneous liquid water path, the total water specific humidity, the temperature, the liquid water content and the liquid water potential temperature fields in the middle of a stratocumulus cloud layer after 8 hours of simulation time on a large horizontal domain (25.6×25.6 km^2). The fields were obtained from a large-eddy simulation of the diurnal cycle of stratocumulus off the coast of California as observed during FIRE I. The results show that the large-scale structures are nearly identical.

Figure 2: The simulated diurnal cycle of the cloud top and cloud base heights (upper panel) and the liquid water path (lower panel). The results were obtained from hourly instantaneous simulated stratocumulus cloud fields. The thick solid lines indicate the mean values, the dashed lines show one standard deviation from the mean, and the dash-dot lines show the minimum and maximum values in the LES domain.

Figure 3: Thumbnail time series of LWP probability density functions. The solid lines indicate PDFs which were computed directly from the 3D LES liquid water content fields, and the dashed lines represent reconstructed PDFs based on the total specific humidity fields in middle of the cloud layer at 450 m according to Eq. (26). The vertical solid lines indicate the mean LWPs.

Figure 4: The skewness of the cloud liquid water path and total specific humidity in the middle of the cloud layer as a function of time. The line styles are explained in the legend.

Figure 5: Energy density spectra of the liquid water path. The results were obtained from the LES fields at t=8, 12, 24 and 36 Local Time.

Figure 6: Energy density spectra of the temperature (T), total water specific humidity (q_t in

g kg^{-1}) and the virtual potential temperature (θ_v) in the (a) middle of the subcloud layer at 210 m and (b) in the middle of the cloud layer at 450 m. Panel (c) shows the spectral correlation of the temperature in the middle of the subcloud layer and in the middle of the cloud layer, respectively. The results were obtained from the LES fields at t=36 Local Time.

Figure 7: Scatter plots of the total specific humidity q_t in the middle of the cloud layer and the liquid water path (a) during the night at $t = 24$ Local Time and (b) during day-time at $t = 36$ Local Time.

Figure 8: Scatter plots of total specific humidity q_t' and temperature T' fluctuations in the middle of the cloud layer (a) during the night at $t = 24$ Local Time and (b) during day-time at $t = 36$ Local Time. The straight line indicates a linear regression fit.

Figure 9: Probability density functions for the total water specific humidity (black lines) and the liquid water content (grey lines) at five different heights in the cloud layer. Panel (a) shows the results during the night at $t = 24$ Local Time and (b) during day-time at $t = 36$ Local Time. Line styles are explained in the legend in panel (a).

Figure 10: The liquid water potential temperature variance $\overline{\theta_l'^2}$ multiplied by a factor A_w^2 and the temperature variance $\overline{T'^2}$ in the middle of the cloud layer as a function of the local time.

Figure 11: Time series of the β factor according to Eq. (8) computed from the temperature and total specific humidity fields in the middle of the cloud layer. The two lines indicated by $T' = 0$ and $\theta_l' = 0$ correspond to the theoretical solutions for β if either temperature or liquid water potential temperature fluctuations are neglected, respectively.

Figure 12: Contour plot of the parameter R defined by Eq. (16) as a function of the inversion jumps $\Delta\theta_l$ and Δq_t.

Figure 13: Scatter plots of liquid water content fluctuations q_l' in the middle of the cloud layer and the subcolumn vertical cloud mean value $[q_l']$ (a) during the night at $t = 24$ Local Time and (b) during day-time at $t = 36$ Local Time.

Figure 14: Schematic illustration of an assumed mean state for which the mean liquid water content $\overline{q_l}$ follows a psuedo-adiabatic vertical profile with slope α. Given height-independent fluctuations of the liquid water content $q_l' = \beta q_t'$, subcolumn vertical liquid water profiles are computed by assuming that they are dictated by the same mean slope α. All cloudy subcolumns are assumed to have the same mean cloud-top height. A vertical integration of the subcolumn liquid water vertical profile yields the subcolumn liquid water path.

Figure 15: (a) The inhomogeneity factor χ computed from instantaneous LES cloud fields. The solid line indicates results obtained from a delta-Eddington radiative transfer model, and the dotted line denotes results computed from I3RC Monte Carlo calculations. A fixed solar zenith angle $\theta_0 = 53^0$ was used. Panel (b) shows the standard deviation of the optical depth, σ_τ, normalized by its mean value $\overline{\tau}$.

Figure 16: Isolines of albedo bias factor χ as a function of the mean optical thickness $\overline{\tau}$ and its normalized standard deviation $\sigma_\tau/\overline{\tau}$. To compute the inhomogeneity factor χ a Gaussian distribution for τ was assumed.

Figure 17: (a) The horizontal slab-mean variance of the optical depth and (b) the horizontal slab-mean albedo bias factor χ as a function of the subdomain size of the LES model. The mean values were computed by averaging over all subdomain results of the instantaneous cloud field at $t = 36$ Local Time.

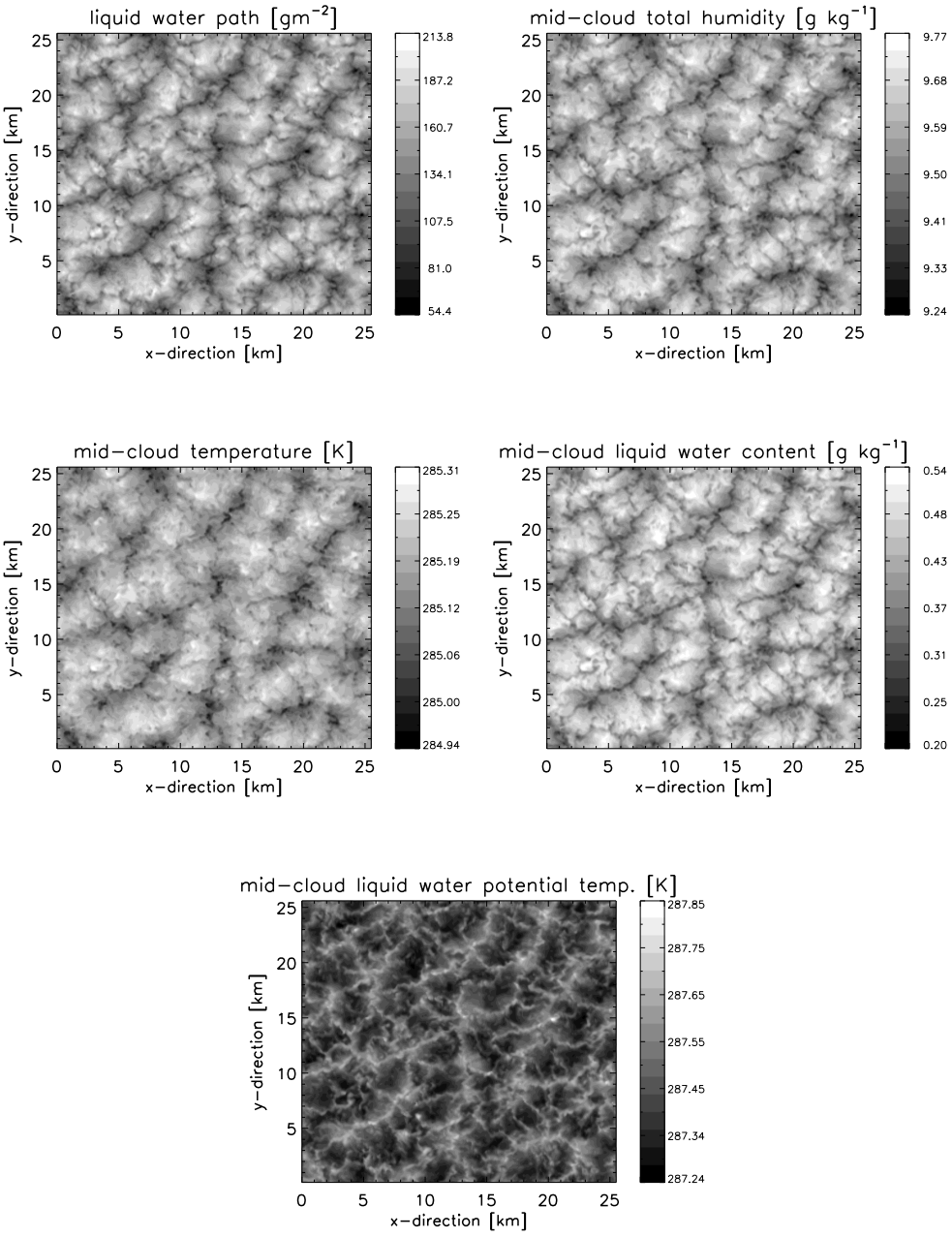
liquid water path [gm^{-2}]
213.8
187.2
160.7
134.1
107.5
81.0
54.4
mid−cloud total humidity [g kg^{-1}]
9.77
9.68
9.59
9.50
9.41
9.33
9.24
mid−cloud temperature [K]
285.31
285.25
285.19
285.12
285.06
285.00
284.94
mid−cloud liquid water content [g kg^{-1}]
0.54
0.48
0.43
0.37
0.31
0.25
0.20
mid−cloud liquid water potential temp. [K]
287.85
287.75
287.65
287.55
287.45
287.34
287.24
y−direction [km]
x−direction [km]
0
5
10
15
20
25

Figure 1:

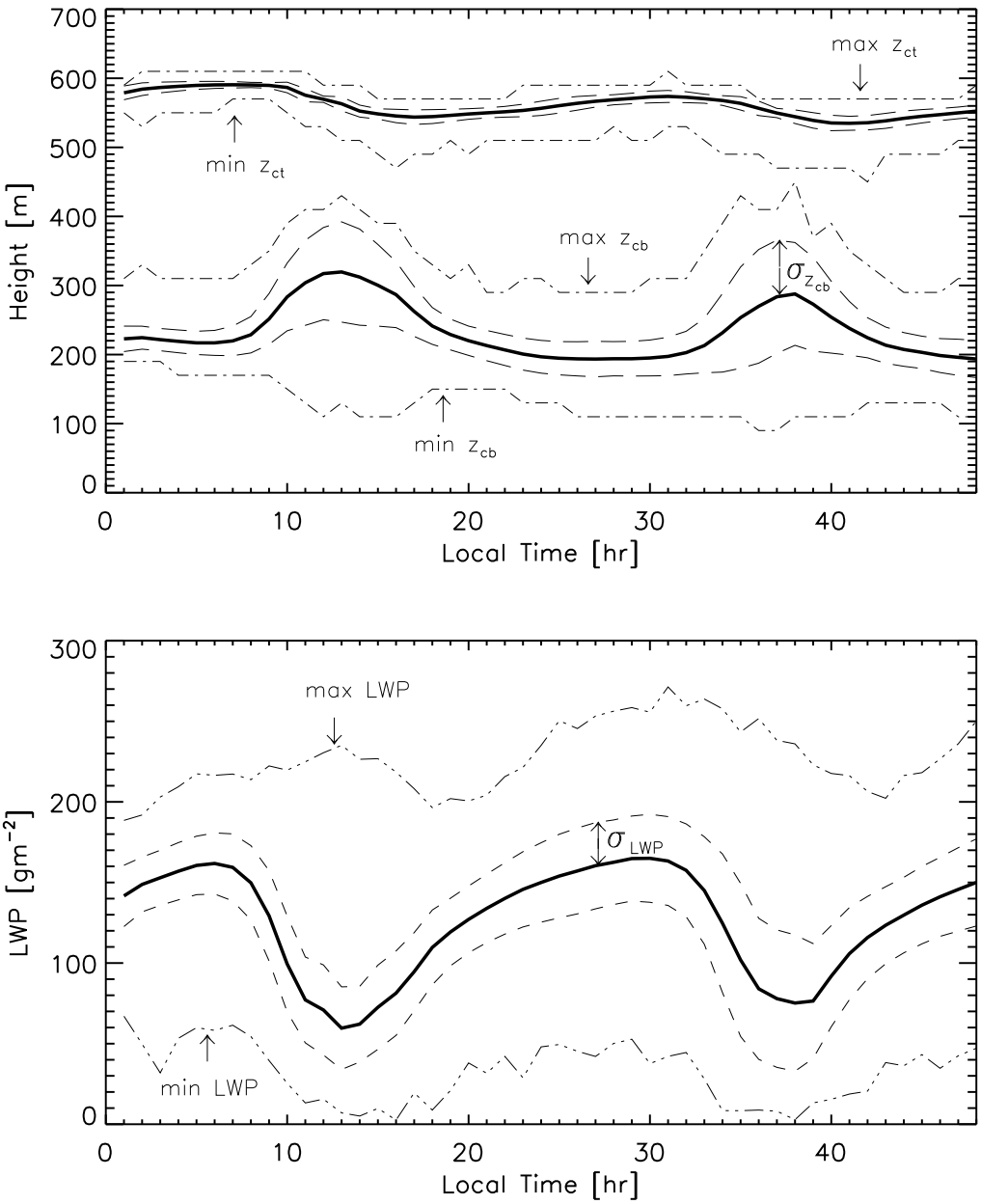
700
600
500
400
300
200
100
0
Height [m]
max z_{ct}
min z_{ct}
max z_{cb}
$\sigma_{z_{cb}}$
min z_{cb}
0
10
20
30
40
Local Time [hr]
300
200
100
0
LWP [gm^{-2}]
max LWP
σ_{LWP}
min LWP
0
10
20
30
40
Local Time [hr]

Figure 2:

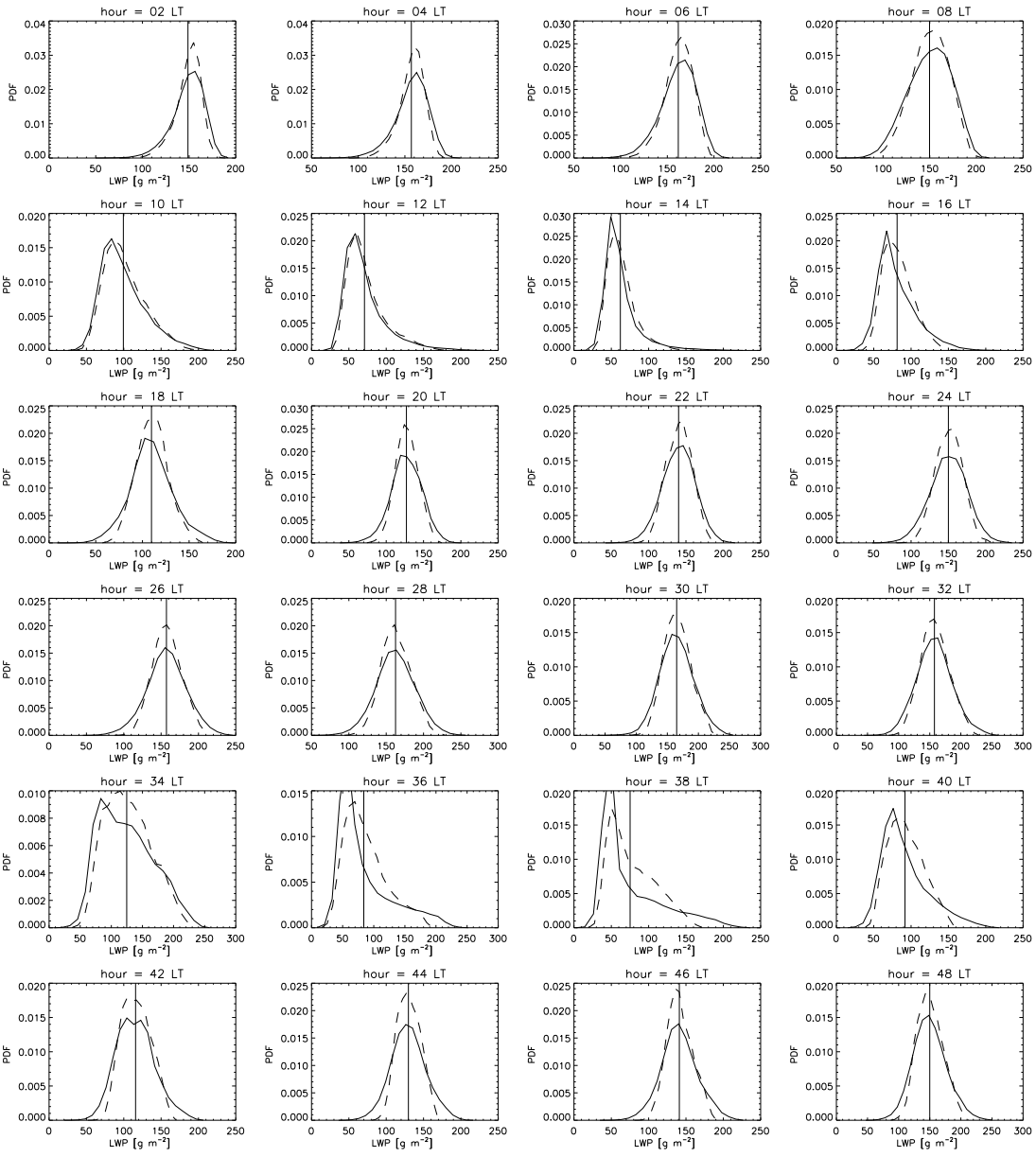
hour = 02 LT
hour = 04 LT
hour = 06 LT
hour = 08 LT
hour = 10 LT
hour = 12 LT
hour = 14 LT
hour = 16 LT
hour = 18 LT
hour = 20 LT
hour = 22 LT
hour = 24 LT
hour = 26 LT
hour = 28 LT
hour = 30 LT
hour = 32 LT
hour = 34 LT
hour = 36 LT
hour = 38 LT
hour = 40 LT
hour = 42 LT
hour = 44 LT
hour = 46 LT
hour = 48 LT
PDF
LWP [g m^{-2}]

Figure 3:

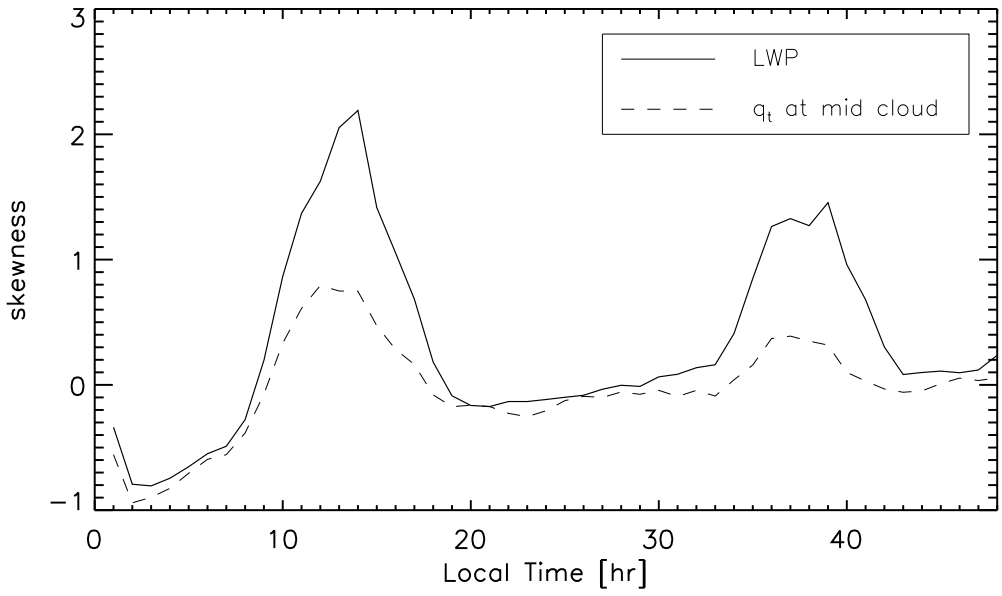

Figure 4:

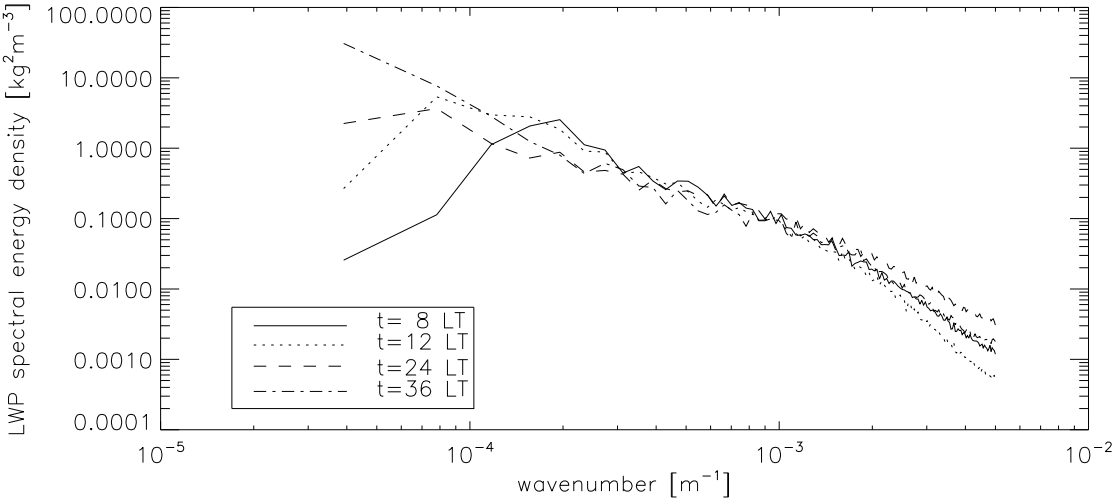
LWP spectral energy density [kg^{2}m^{-3}]
100.0000
10.0000
1.0000
0.1000
0.0100
0.0010
0.0001
10^{-5}
10^{-4}
10^{-3}
10^{-2}
wavenumber [m^{-1}]
t= 8 LT
t=12 LT
t=24 LT
t=36 LT

Figure 5:

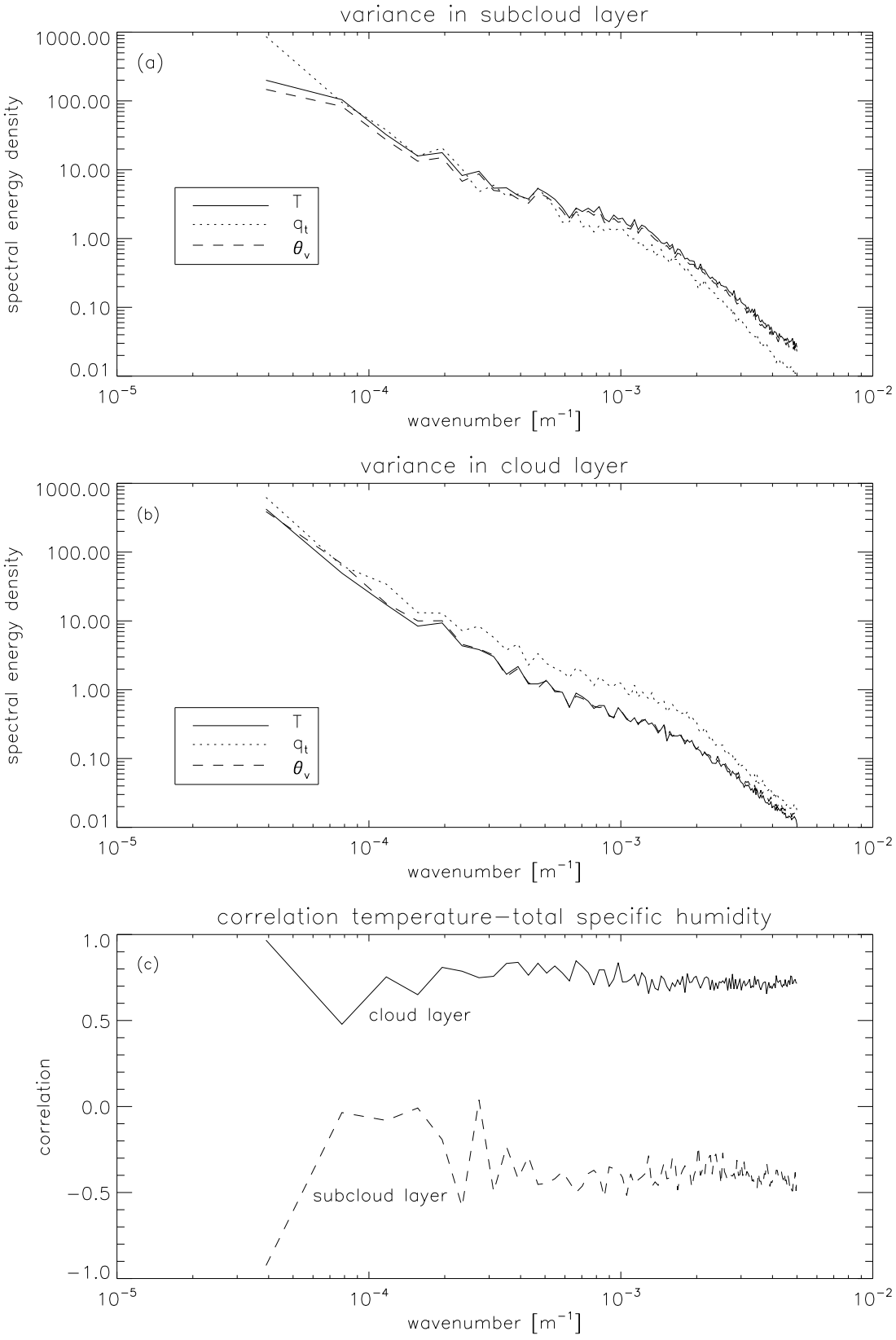
variance in subcloud layer
(a)
spectral energy density
1000.00
100.00
10.00
1.00
0.10
0.01
T
q_t
θ_v
10^{-5}
10^{-4}
10^{-3}
10^{-2}
wavenumber [m^{-1}]
variance in cloud layer
(b)
spectral energy density
1000.00
100.00
10.00
1.00
0.10
0.01
T
q_t
θ_v
10^{-5}
10^{-4}
10^{-3}
10^{-2}
wavenumber [m^{-1}]
correlation temperature−total specific humidity
(c)
correlation
1.0
0.5
0.0
−0.5
−1.0
cloud layer
subcloud layer
10^{-5}
10^{-4}
10^{-3}
10^{-2}
wavenumber [m^{-1}]

Figure 6:

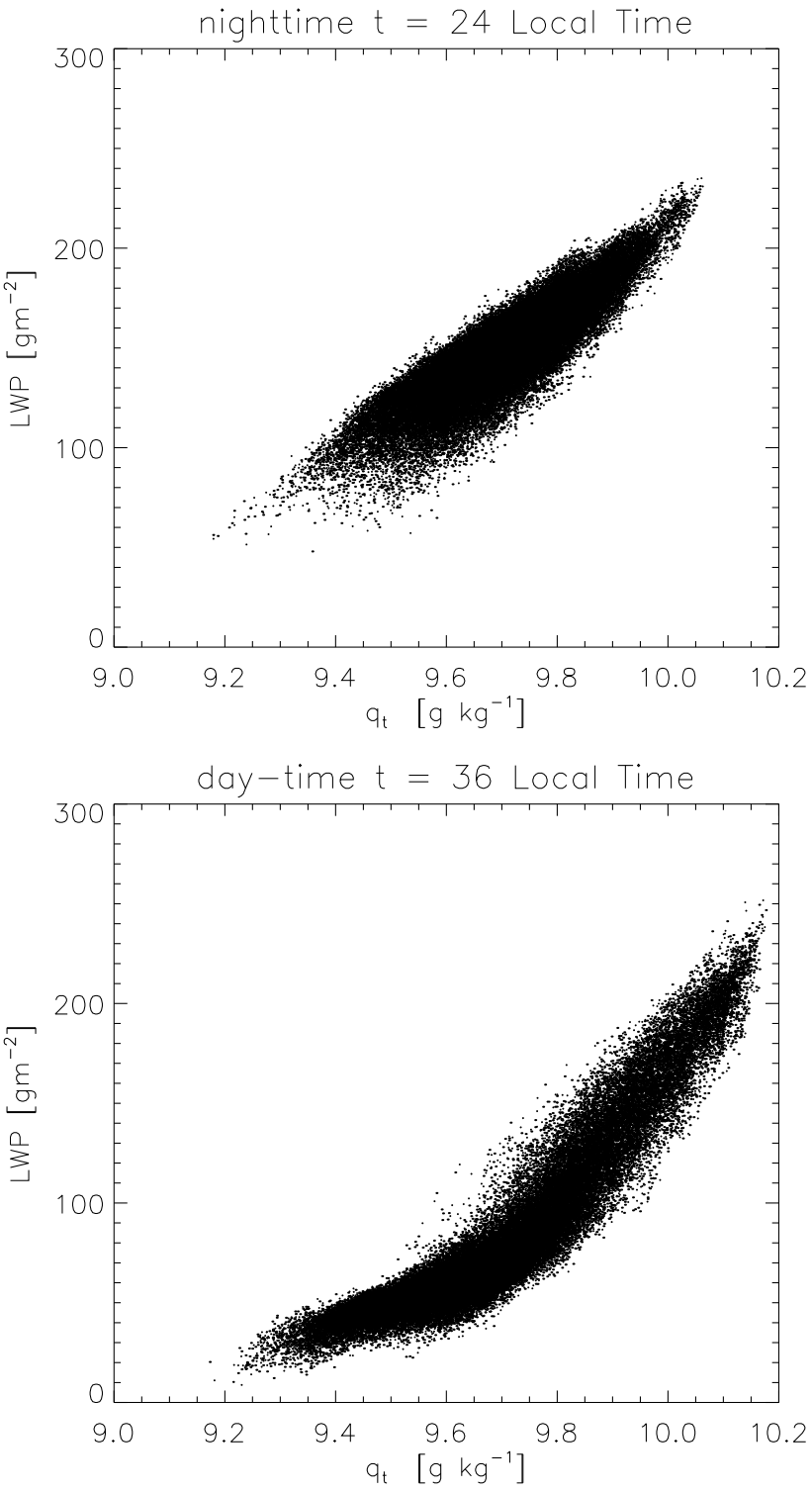
nighttime t = 24 Local Time
LWP [gm^{-2}]
300
200
100
0
9.0
9.2
9.4
9.6
9.8
10.0
10.2
q_t [g kg^{-1}]
day−time t = 36 Local Time
LWP [gm^{-2}]
300
200
100
0
9.0
9.2
9.4
9.6
9.8
10.0
10.2
q_t [g kg^{-1}]

Figure 7:

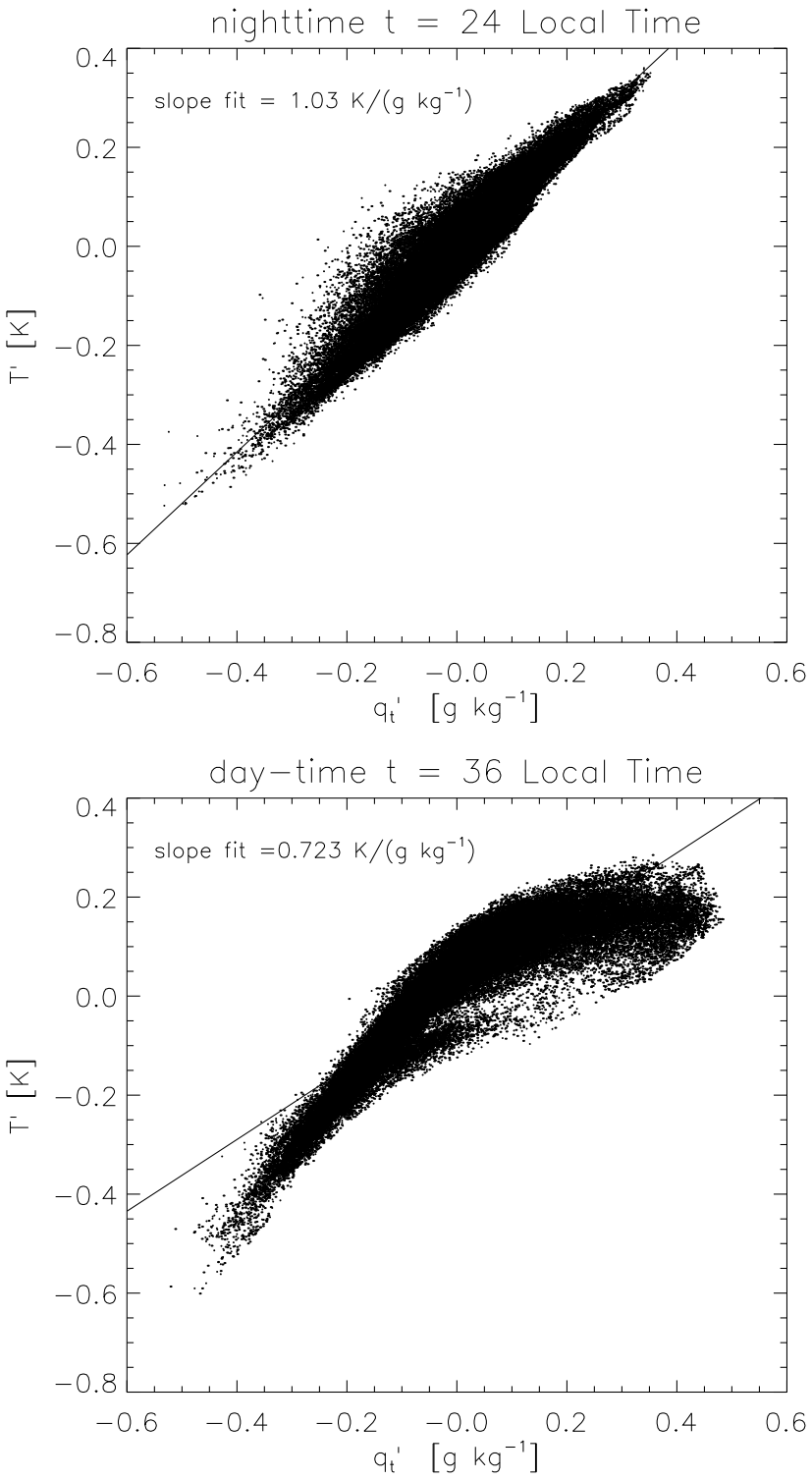
nighttime t = 24 Local Time
slope fit = 1.03 K/(g kg^{-1})
T' [K]
q_t' [g kg^{-1}]
day−time t = 36 Local Time
slope fit =0.723 K/(g kg^{-1})
T' [K]
q_t' [g kg^{-1}]

Figure 8:

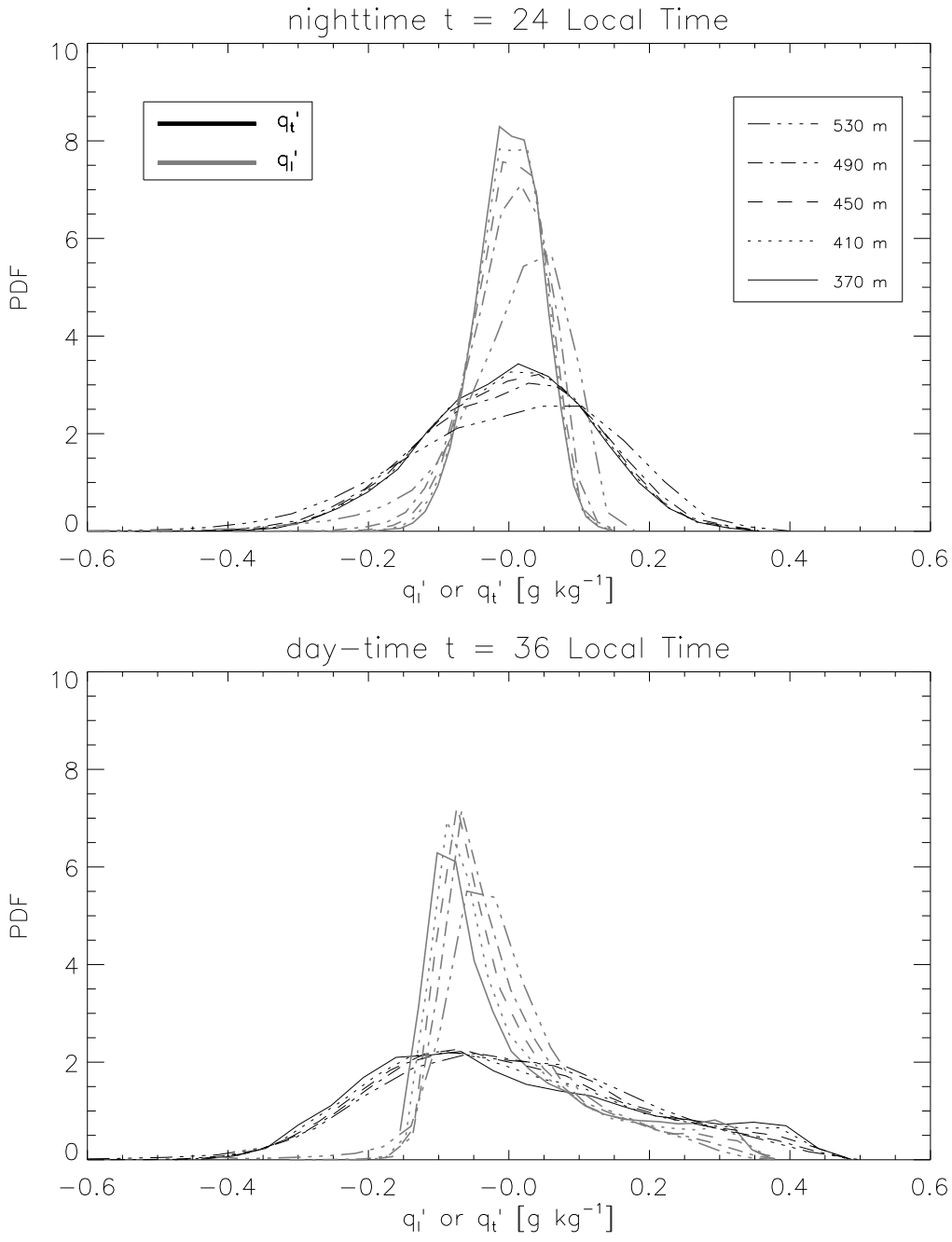
nighttime t = 24 Local Time
PDF
q_t'
q_l'
530 m
490 m
450 m
410 m
370 m
q_l' or q_t' [g kg^{-1}]
day−time t = 36 Local Time
PDF
q_l' or q_t' [g kg^{-1}]

Figure 9:

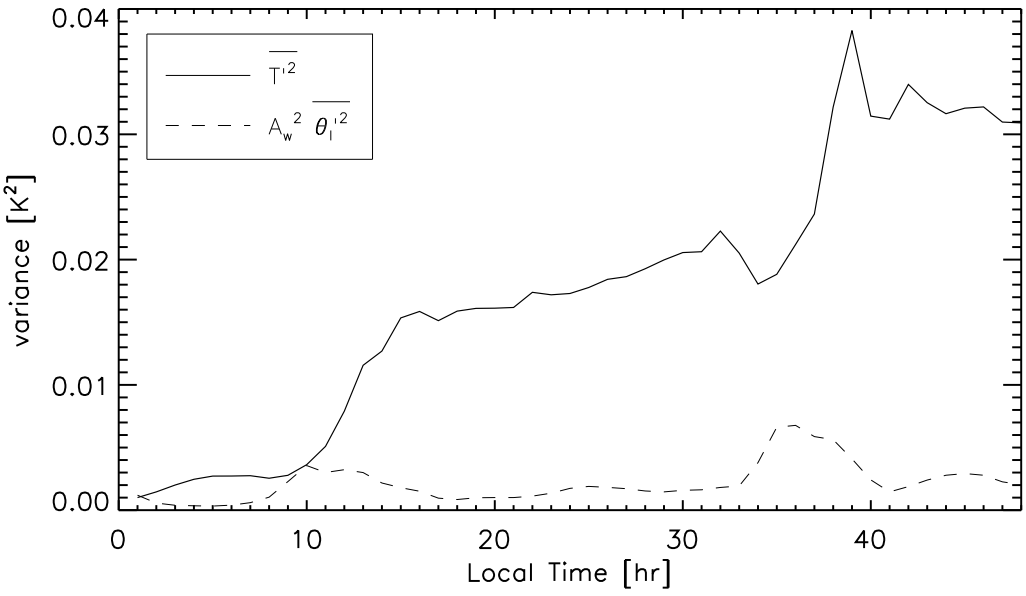
0.04
0.03
0.02
0.01
0.00
variance [K²]
0
10
20
30
40
Local Time [hr]
$\overline{T'^2}$
$A_w^2\ \overline{\theta_l'^2}$

Figure 10:

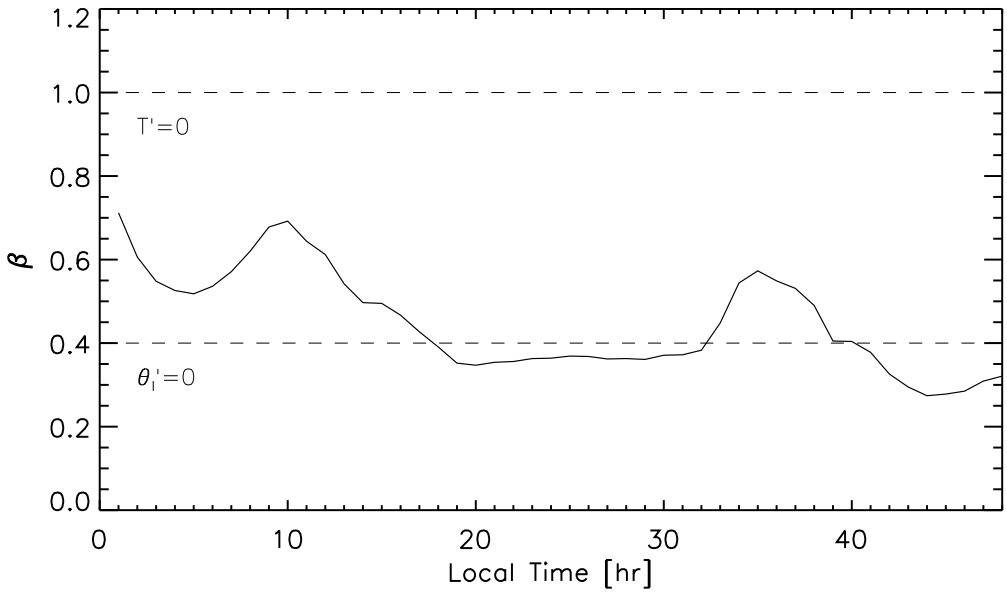

Figure 11:

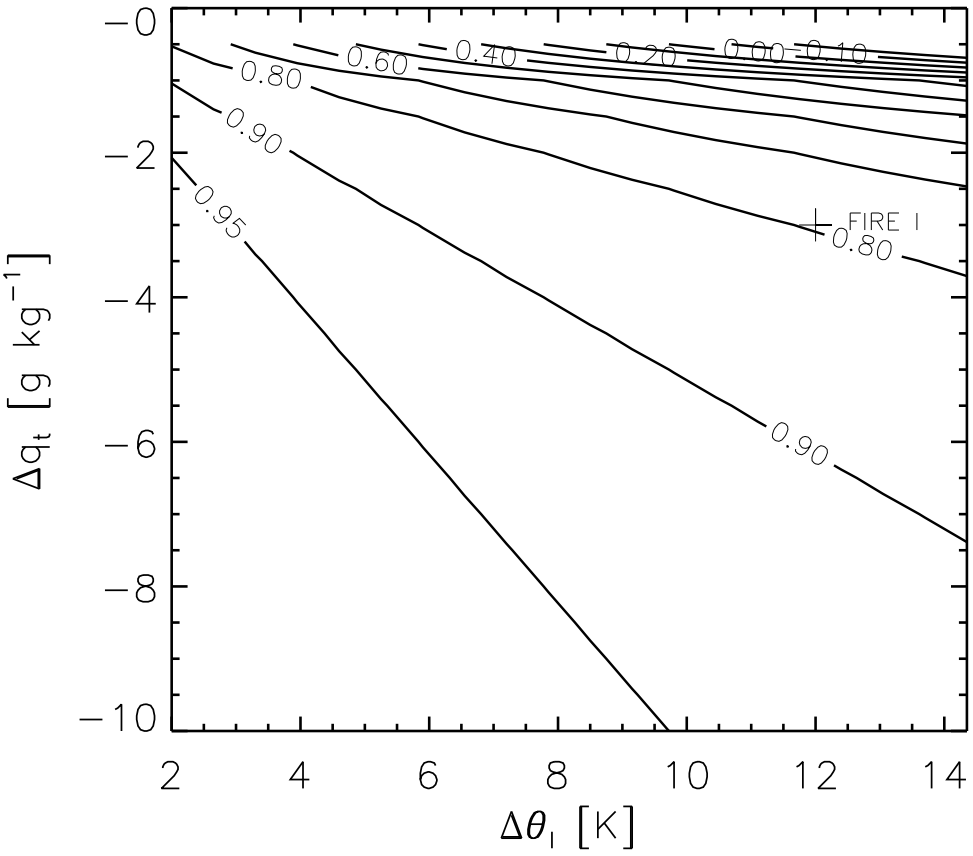
0.80
0.60
0.40
0.20
0.00
0.10
0.90
0.95
FIRE I
0.80
0.90
−0
−2
−4
−6
−8
−10
2
4
6
8
10
12
14
Δq_t [g kg^{-1}]
$\Delta\theta_l$ [K]

Figure 12:

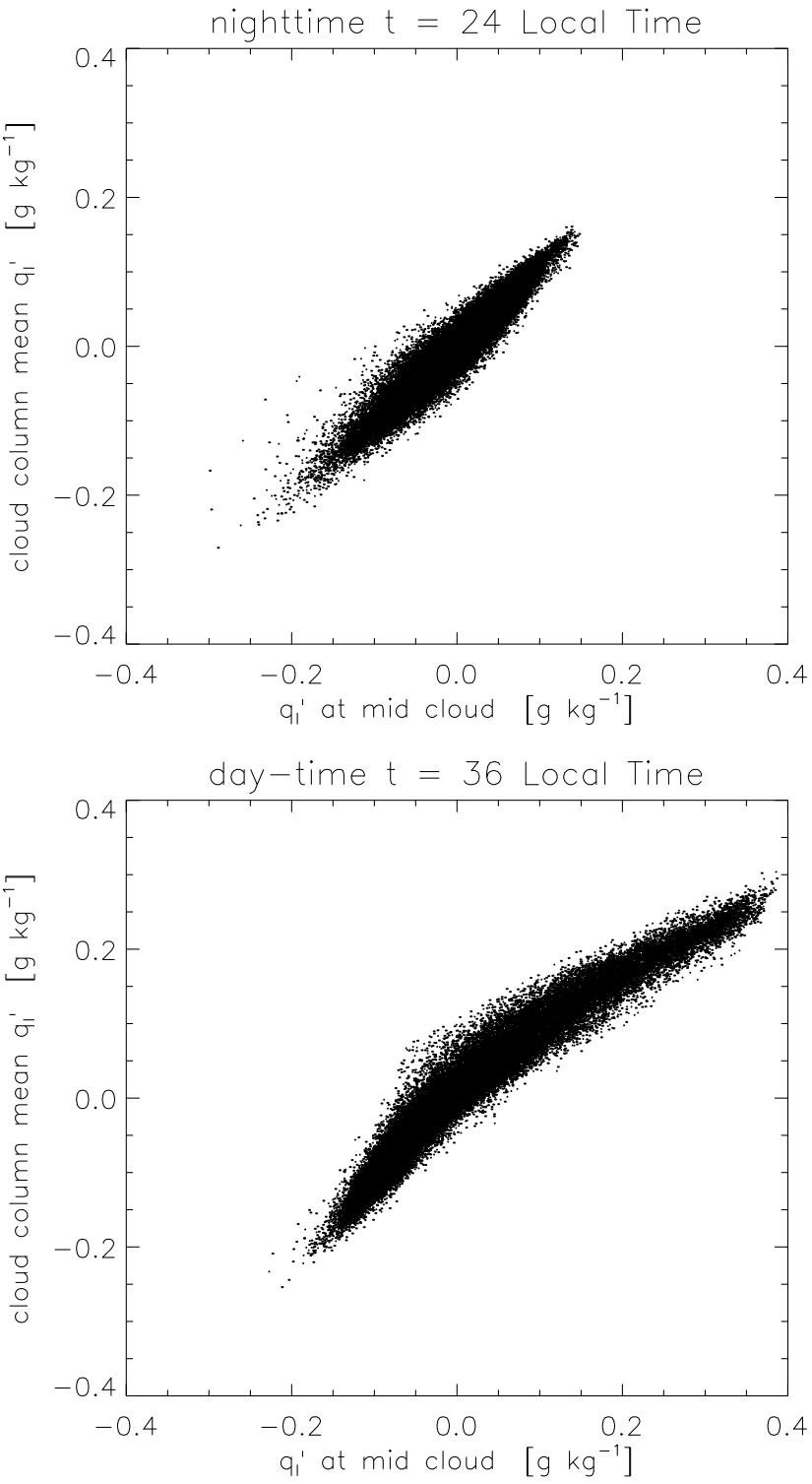
nighttime t = 24 Local Time
cloud column mean q_l' [g kg^{-1}]
q_l' at mid cloud [g kg^{-1}]
0.4
0.2
0.0
−0.2
−0.4
day−time t = 36 Local Time
cloud column mean q_l' [g kg^{-1}]
q_l' at mid cloud [g kg^{-1}]

Figure 13:

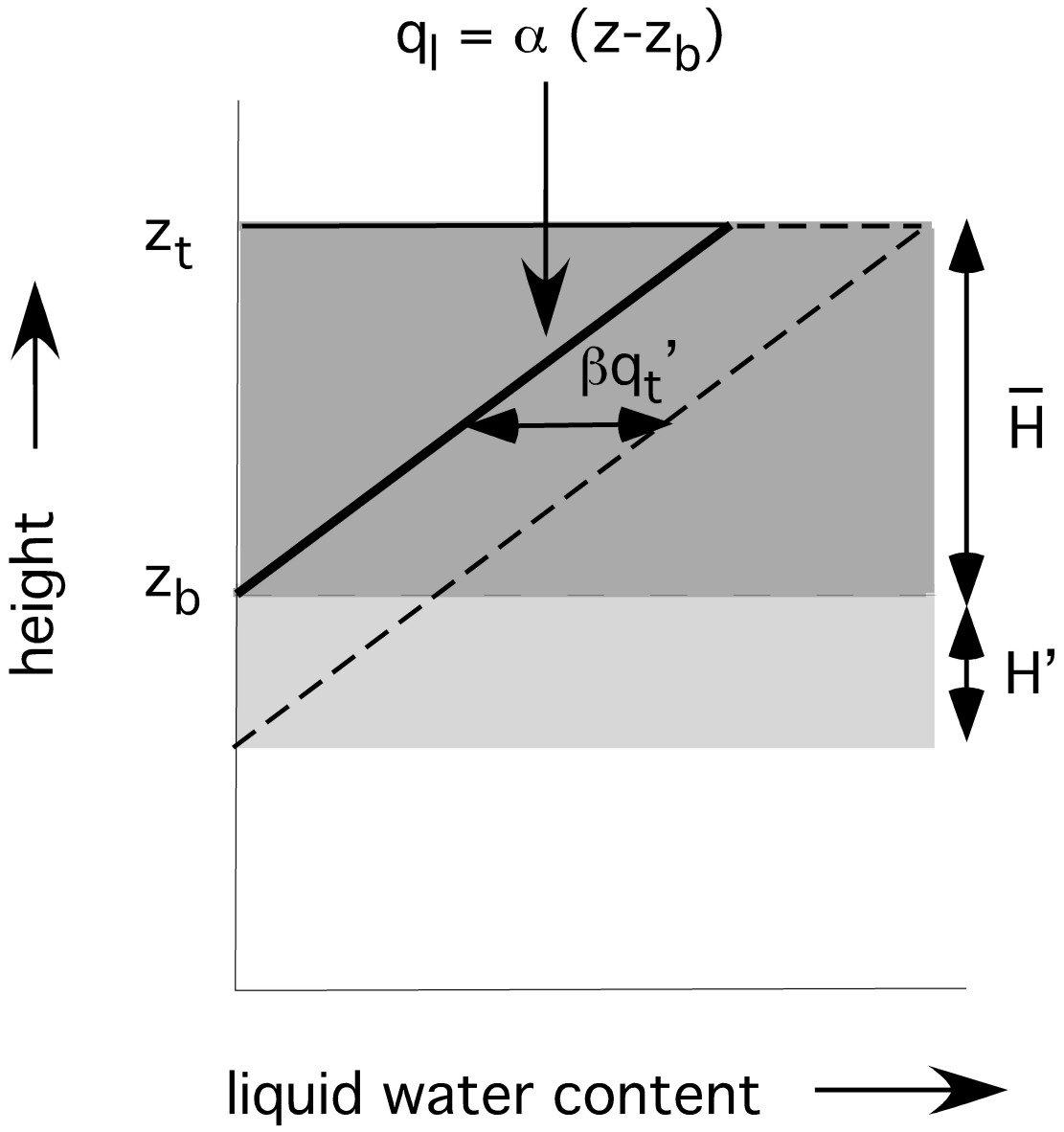
$q_l = \alpha\ (z\text{-}z_b)$
z_t
$\beta q_t'$
$\bar{H}$
z_b
H'
height
liquid water content

Figure 14:

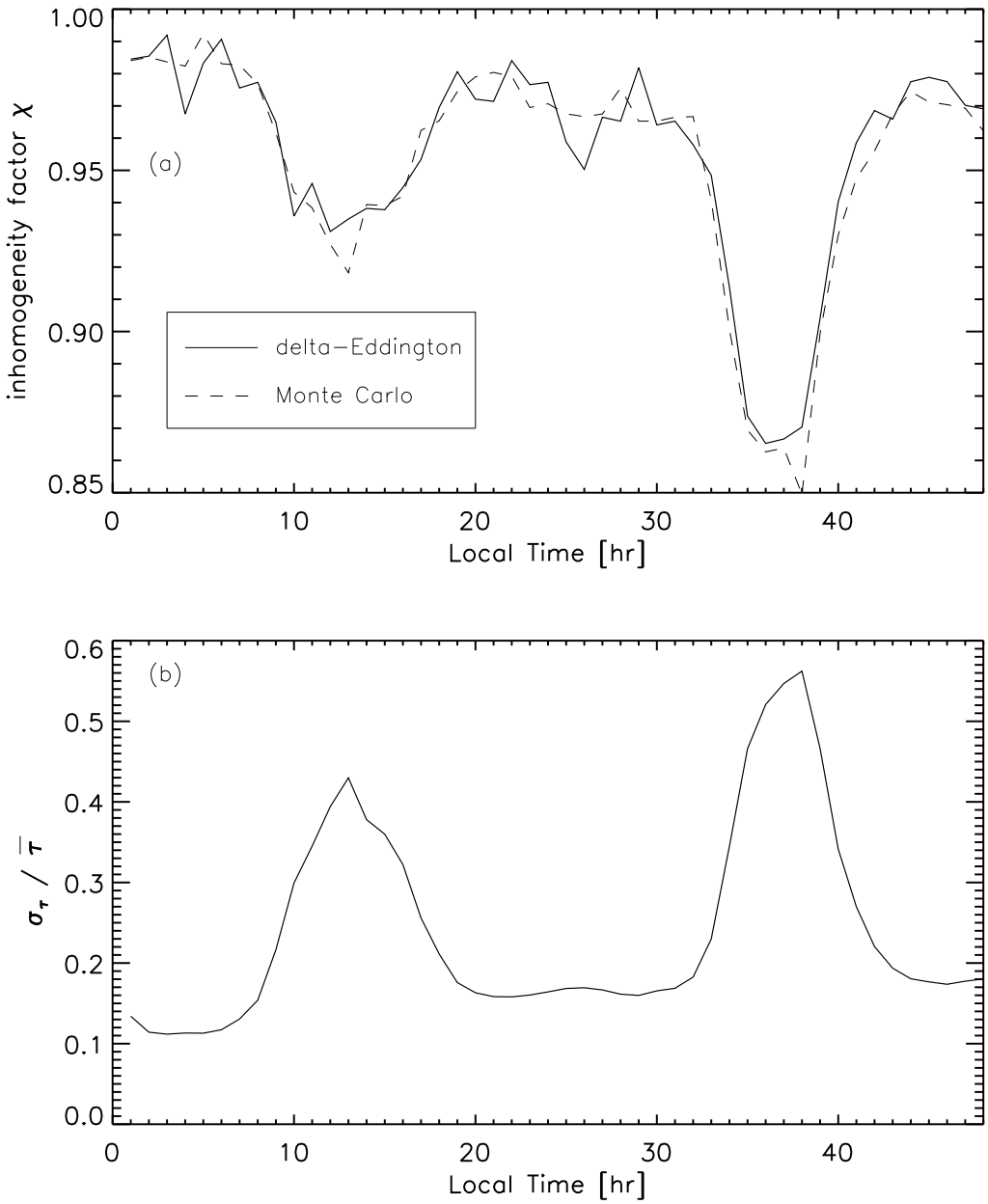
1.00
0.95
0.90
0.85
inhomogeneity factor χ
(a)
delta−Eddington
Monte Carlo
0
10
20
30
40
Local Time [hr]
0.6
0.5
0.4
0.3
0.2
0.1
0.0
(b)
Local Time [hr]

Figure 15:

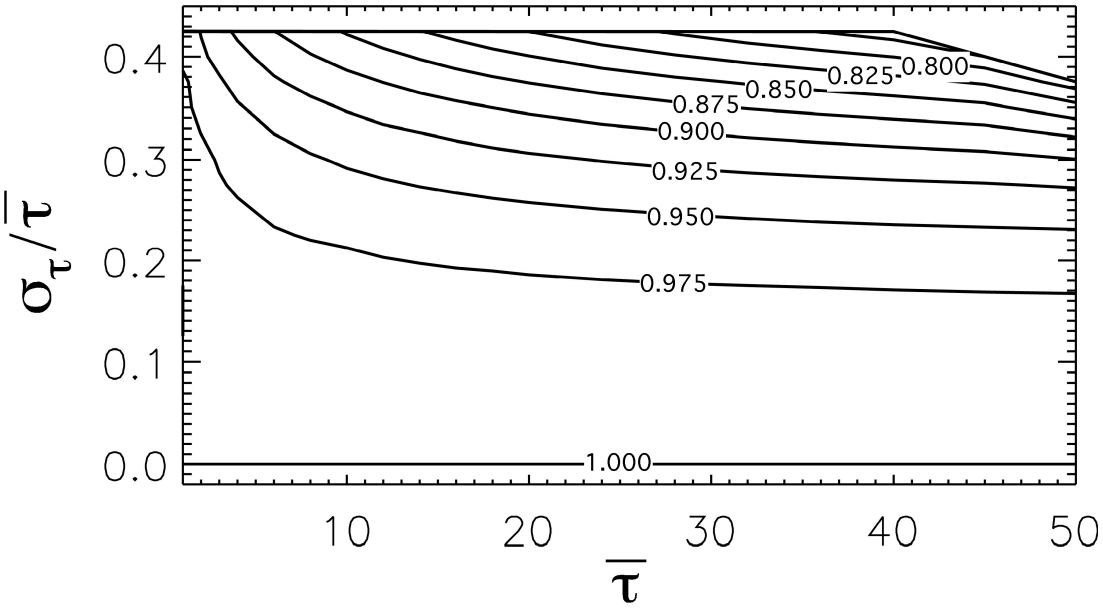
0.4
0.3
0.2
0.1
0.0
$\sigma_\tau/\overline{\tau}$
0.800
0.825
0.850
0.875
0.900
0.925
0.950
0.975
1.000
10
20
30
40
50
$\overline{\tau}$

Figure 16:

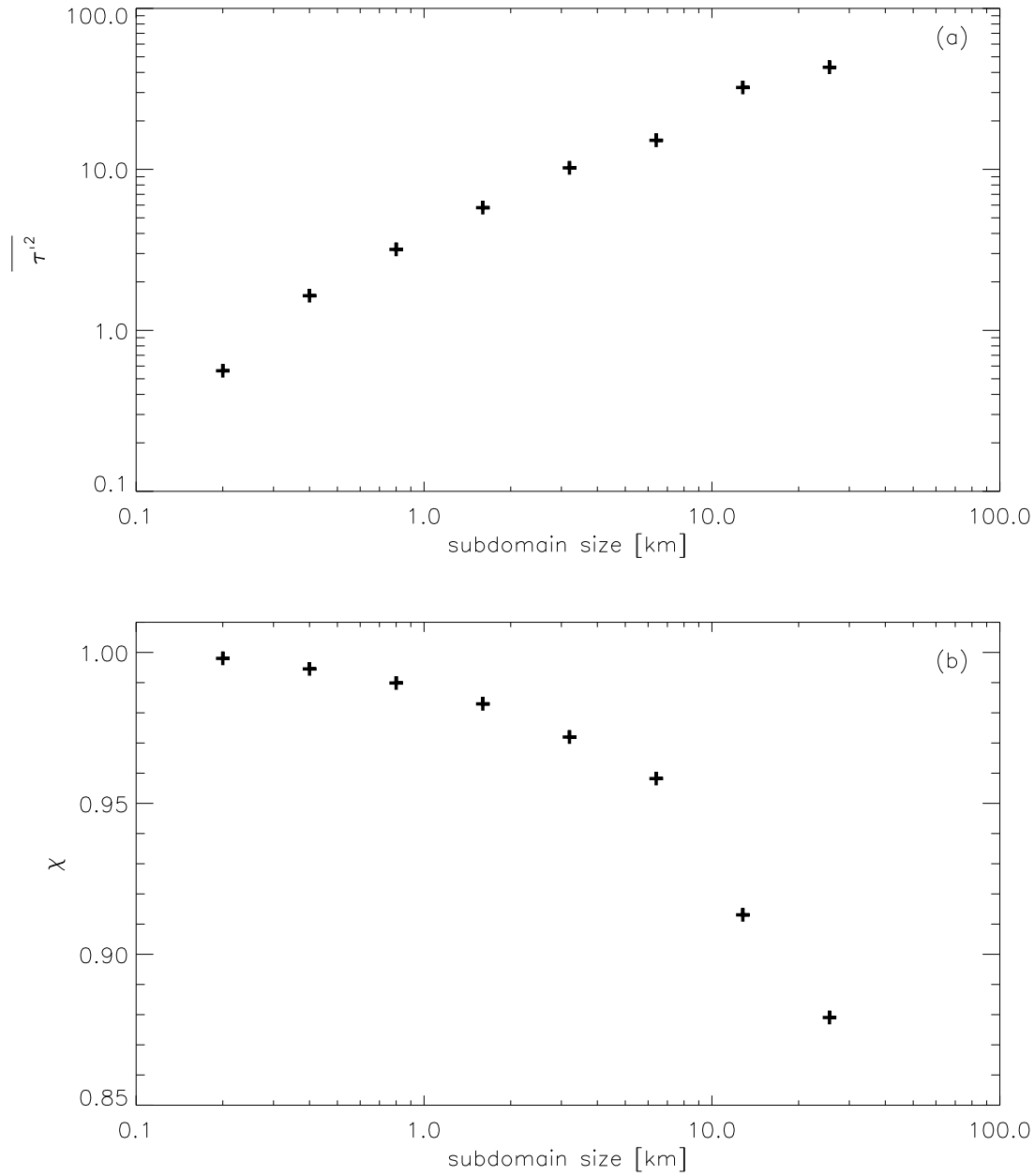
100.0
10.0
1.0
0.1
(a)
$\overline{\tau'^2}$
0.1
1.0
10.0
100.0
subdomain size [km]
1.00
0.95
0.90
0.85
(b)
χ
0.1
1.0
10.0
100.0
subdomain size [km]

Figure 17: